Multiscale characterisation of single synthetic fibres: *Surface morphology and nanomechanical properties*

Dajana Gubała [1], Robert Harniman [1], Jean-Charles Eloi [1], Patryk Wąsik [1,2,♦], Didier Wermeille [3,4], Lili Sun [5], Eric Robles [6], Meng Chen [5], Wuge H. Briscoe [1]*

[1] School of Chemistry, University of Bristol, Cantock's Close, Bristol BS8 1TS, UK

[2] Bristol Centre for Functional Nanomaterials, HH Wills Physics Laboratory, University of Bristol, Bristol, BS8 1TL, UK

[3] XMaS, the UK-CRG, European Synchrotron Radiation Facility (ESRF), 71 avenue des Martyrs, BP 220, 38043 Grenoble CEDEX 9, France

[4] Department of Physics, University of Liverpool, The Oliver Lodge Laboratory, Liverpool L69 7ZE, UK

[5] Procter & Gamble Beijing Innovation Centre, 35 Yu'an Rd, Shunyi District, Beijing 101312, China

[6] Household Care Analytical, Procter & Gamble Newcastle Innovation Centre, Whitley Road, Longbenton, Newcastle, NE12 9TS, UK

♦ Present address: National Synchrotron Light Source II, Brookhaven National Laboratory, Upton, New York 11973, USA

** E-mail: wuge.briscoe@bristol.ac.uk; Tel: +44 (0)117 3318256*

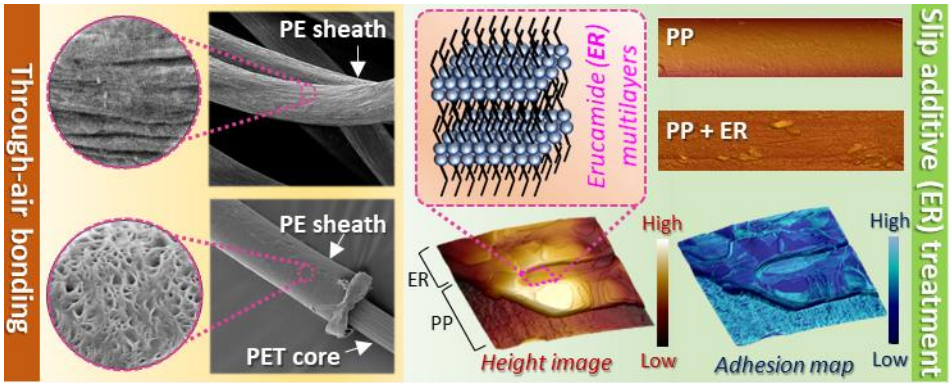

Abstract

Hypothesis: Thermal through-air bonding process and slip additive treatment affect fibre surface structure and nanomechanical properties, which is extremely difficult to characterise on a single-fibre level.

***Experiments*:** Optical microscopy (OM) was applied to study the effect of air-through bonding, spunbonding, and crimping on fibre geometry and general appearance. A "spray-on" method developed here using a custom-designed fibre holder allowed a direct measurement of *static* contact angles of water droplets on single fibres. Scanning electron microscopy (SEM) showed different morphological features on the fibre due to the nonwoven fabric-making process and additive treatment. Synchrotron X-ray diffraction (XRD) was applied to study the effect of erucamide presence on polypropylene (PP) fibre crystal structure. Atomic force microscopy (AFM) imaging provided complementary characterization of fibre topographic features such as average surface roughness, along with adhesion force mapping by quantitative nanomechanical (QNM) AFM imaging.

***Findings*:** Our results show the effect of nonwoven making process and surfactant additive treatment on the fibre surface structure and nanomechanical properties. Wettability experiment on the single fibre revealed the hydrophobic nature of all the synthetic fibres. For polyethylene/polyethylene terephthalate (PE/PET) bicomponent single fibres, the polyethylene sheath was found to possess fibrillar microstructure - typical for drawn fibres, whereas the fibres entangled in nonwoven fabrics exhibited a uniform, porous surface morphology attributed to the through-air process. Adhesion force mapping allowed us to correlate fibre nanomechanical properties with its topography, with surface pore interiors showing higher adhesion than the flat polyethylene region. Furthermore, on the polypropylene (PP) fibre surface treated with erucamide (13-*cis*-docosenamide; a common slip additive used in polyolefin film processing), we observed overlapping multilayers consisting of 4 nm erucamide bilayers, attributed to the slip additive migration onto the fibre surface. X-ray diffraction (XRD) measurements of the fibres did not detect the presence of erucamide; however, AFM imaging provided evidence for its migration to the fibre surface, imparting influence on the surface structure and adhesive properties of the fibre. Single-fibre AFM imaging also allowed a detailed analysis of different surface roughness parameters, revealing that both through-air bonding in the nonwoven making process and the slip additive (erucamide) treatment reduced the surface roughness, an effect more pronounced for the PE/PET than the PP fibres. The wettability, surface morphology, and adhesion properties from this study, obtained with unprecedented resolution and details on single fibres, are valuable to informing rational design

of fibre processing for fibre optimal properties, critically important in many industrial applications.

Keywords

Polymer fibres; nonwovens; softness; surface characterisation; erucamide; single fibres; "blooming" process; fibre crimping

Introduction

Synthetic fibres have been widely used in nonwoven fabrics in many applications, ranging from hygiene and health care products to automobile protective covers [1-8]. Synthetic fibres made from polyolefins such us polyethylene and polypropylene, when in a raw state, often exhibit rough, tacky surfaces of high friction, which can affect not only their processing (*e.g*. causing fibre breakage and production inconsistency) but also the properties and consumer perceptions of the final product (*e.g.* softness, strength, and general appearance). Several approaches have been developed to modify surface chemistry [9-11] and morphology [12, 13] of polymer fibres and fabrics, and to improve their dyeing efficiency [14, 15] and antimicrobial properties [16, 17]. For synthetic fibres used in nonwoven materials for personal care products (*e.g.* babies' nappies and female sanitary pads) or medical products (swabs and surgical masks), fibre softness is a key consumer satisfaction criterion, due to the intimate contact of the product with delicate and sensitive anatomical parts of the human body.

The incorporation of small organic molecules (*i.e.* slip additives) at low concentration has a great potential to tailor material tactile properties. For instance, surfactants can be added (as slip additives) during polymer extrusion in fibre fabrication, which then can migrate to the polymer surface and form a solid lubricating layer (a process termed "blooming"), moderating polymer fibre friction and adhesion properties [18, 19]. Slip additive migration, distribution

and efficiency in friction reduction is highly dependent on the nature of additives (*e.g.* their molecular weight, shape [20], and concentration [21]) and manufacturing conditions (*e.g.* temperature [22]).

For many years, fatty acid amides have been widely studied and considered as slip agents in the field of polymer film lubrication [23-25]. Erucamide (cis-13-docosenamide; Figure1), known to reduce the polymer film friction coefficient down to 0.2 [26], is currently one of the most widely studied and used such slip additives in the polyolefin film processing industry [27-32]. In comparison to other additives, erucamide not only promotes favourable slip properties, but also possesses superior heat resistance due to its relatively high melting point (mp 75-80°C) [27].

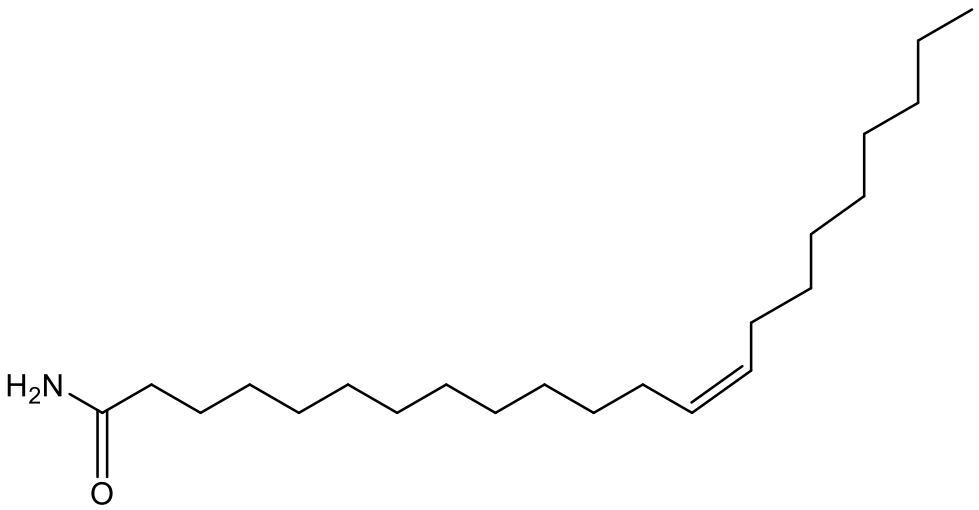

Figure 1 Erucamide chemical structure.

Another approach to impart material softness involves modification of fibre geometry by *crimping*, characterised as the degree of deviation from the linearity of a non-straight fibre imparted mechanically, chemically or during fibre growth (self-crimping) [33]. Crimping facilitates separation between fibres in a fabric, introduces loftiness, and also affects fibre cohesion as well as cross-fibre friction. This can help synthetic fibres imitate the properties of natural fibres, therefore allowing for their processing with conventional equipment.

Furthermore, the crimp can facilitate separation between fibres and machinery, preventing wastage caused by fibre adherence to the mechanical equipment, allowing for better processing efficiency and consistency. Unfortunately, changing the fibre geometry is often accompanied by its mechanical strength reduction due to stress concentration at the crimp under stress, making the fibre more vulnerable to breakage [34].

The aforementioned strategies have largely derived from fibre manufacturers' empirical wisdoms and consumers' feedback, and their implementation is time-consuming and costly. Detailed fibre characterisation, particularly of its surface morphology and nanomechanical properties, is very challenging due to the complex fibre geometry and surface texture. Such knowledge can bring advances towards a better understanding of the relationship between fibre manufacturing and its properties, as well as providing guidance for improvement of tuning tactile qualities for such materials.

In this context, optical microscopy (OM), scanning electron microscopy (SEM), and atomic force microscopy (AFM) are useful tools for the investigation of fibre surface properties and widely used for studying the effectiveness of various fibre surface treatment [35-42]. Here, we have used OM, SEM, and AFM to characterise the topography of six polymer fibres originated from three different suppliers. Since human tactile discrimination can extend down to a few nm [43], characterisation of fibres surface nanostructure and nanomechanical properties is highly relevant. Adhesion force mapping with Peak force Quantitative Nanomechanical Mapping (QNM) technology, less commonly employed in fibre characterisation, has been used here, which allowed access to fibre nanomechanical properties with simultaneous imaging of fibre topography with nm scale resolution, facilitating a detailed examination of the effect of fibre surface treatments. The combination of AFM imaging and adhesion force QNM is of

particular value in the assessment of the differences in fibre adhesion properties, allowing for the correlation between the exhibited adhesion force and specific surface features. The study showcases the feasibility of using these advanced imaging, force, and structure characterisation techniques to study fibres, yielding information with unprecedented details and insights on surface morphology and nanomechanical properties of synthetic fibres.

Materials and methods

Six polymer fibres investigated (Table 1) were kindly donated by Procter & Gamble (Beijing). Samples 1-4 were bi-component, made of polyethylene terephthalate (PET) and polyethylene (PE) at a mass ratio of *ca.* 50:50, with samples 2 and 4 being staple fibres. Samples 1 and 3 were nonwoven fabrics using fibres of samples 2 and 4, respectively, as the starting material made *via* the dry-laid process, which was followed by web bonding *via* the thermal through-air bonding process [44]. Through-air bonding is known as a modern method of passing hot air through unbonded bicomponent fibre surface through negative pressure of suction in order to soften, melt and bond the fibre to form a nonwoven sheet; however the effect of such process on single fibre morphological properties has not been yet established. Samples 5 and 6 were fibres of polypropylene (PP), a homopolymer designed by ExxonMobil™ specifically for spunbonded nonwovens, with Sample 6 also containing 1.5 % of erucamide ($C_{22}H_{43}NO$; Figure 1) per fibre. In order to prepare the samples before each measurement, single fibres were carefully removed from fibre bundles or fabrics with tweezers to minimize any fibre stretching and breakage.

Table 1 Polymer fibres investigated in current work. (a. Supplier information; b. results from this work)

Sample no.	**1**	**2**	**3**	**4**	**5**	**6**

Composition [a]	~50:50 PE/PET sheath/core				PP monofilament	PP monofilament with1.5% erucamide
Assembly[a]	nonwoven fabric	staple fibres	nonwoven fabric	staple fibres	fibres	fibres
Fibre fabrication[a]	carded through-air bonded nonwoven				spunbonded	
Diameter d_f (µm) [b]	**Sheath (total):** 18.4		**Sheath (total):** 16.9		14.2	15.3
	Core: 12.5		**Core:** 10.6			
Crimp frequency/25 mm C_f [a] **[33]**	14.6		14.5		non-crimped	non-crimped
Crimp degree (%) K_g[a]**[33]**	9.6		14.1			
Mean water contact angle[b] **(°)**	124.6 ± 1.2	114.2 ± 1.3	120.3 ± 1.2	124.1 ± 0.6	126.3 ± 0.4	122.4 ± 0.3
Mean droplet volume[b] **(µL)**	0.029 ± 0.010	0.025 ± 0.013	0.022 ± 0.007	0.020 ± 0.006	0.031 ± 0.001	0.034 ± 0.007

Optical microscopy (OM) Optical microscopy (OM) images (magnification ×2) were taken using a Scientifica SliceScope optical microscope equipped with an external camera (902H2 ULTIMATE EIA, Watec, USA).

Fibre wettability Fibre wettability was measured at room temperature (20.5 ± 0.5 °C) using a Drop Shape Analyzer – DSA100 (KRÜSS) operated with KRÜSS ADVANCE 1.9.0.8 software. Static contact angles were measured using MilliQ® water (resestivity of 18.2 MΩ.cm at 25°C) as a probe liquid. It is challenging to use the sessile drop method to measure the

contact angle on fibres, as the water drops formed from the conventional syringe dispenser were unstable on the fibre due to their relatively large volume (and thus gravity). To form sufficiently small droplets, a spray bottle was used to spray water onto fibres stretched across a custom-designed holder (Figure 2a-b) allowing for the formation of multiple droplets of desired volume ~0.03 µL. Typically the images of 10 droplets per fibre were processed with ImageJ software [45] to obtain the droplet diameter (D) and volume (V) and the static contact angle (θ) (*cf.* Figure 2c-d). The contact angle was calculated as follows: the side angle of right triangle ($\alpha = \frac{\theta}{2}$), the height of the formed droplet and (h), and the length of the contact between the sample surface and the droplet (d) can all be obtained from the analysis, with $\tan\alpha = \frac{2h}{d}$. The contact angle can be calculated as $\theta = 2\alpha = 2\tan^{-1}\left(\frac{2h}{d}\right)$.

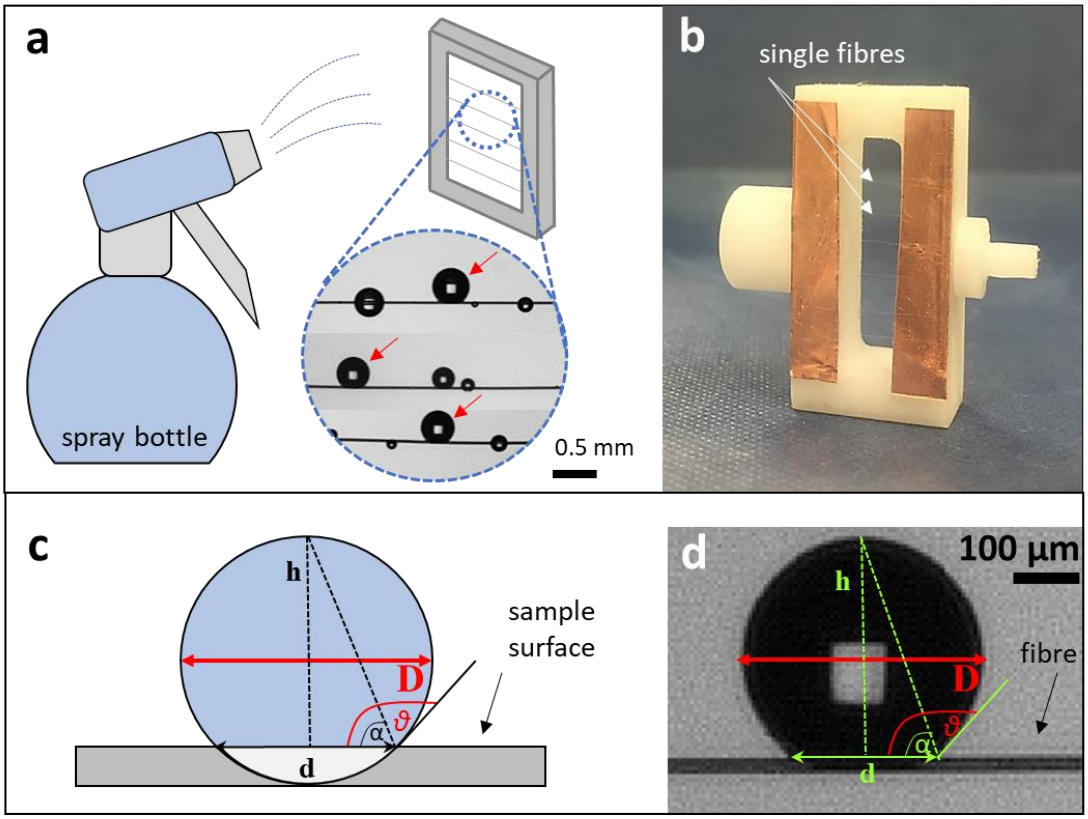

Figure 2 (a) Schematic representation of the contact angle measurement on fibres; b) a photograph of the sample holder with multiple single-fibres mounted horizontally; (c)

schematic representation of the contact angle geometry on a hydrophobic fibre; and (d) an example of a 0.03 μL water droplet on a fibre (sample 6, PP fibre with erucamide).

Scanning Electron Microscopy (SEM) Prior to the measurement, each sample was coated with a ~12 nm silver layer. SEM images were obtained using JSM-IT300 (JEOL, Japan) at the room temperature, with an accelerating voltage of 5kV and a working distance of 9-11 mm. High-resolution SEM images present in Figure 4g-h, Figure 6a1, and Figure S4e-f in SM were obtained using Hitachi S-4800 (Japan) at room temperature, with an accelerating voltage of 3 kV and working distance of ca.8 mm The collected images were processed with ImageJ software [45].

Atomic Force Microscopy (AFM) The fibres were laid flat individually over a circular double-sided sticky carbon pad mounted on a steel sample stub. For each fibre, a straight section was positioned under the cantilever tip viewed via a camera. AFM imaging along the fibres was undertaken using Nanoscope Multimode III microscope with a Nanoscope V controller (Bruker, UK), and NuSense SCOUT cantilevers used had a typical spring constant of 42 Nm^{-1} (NuNano Ltd., UK). Adhesion force mapping and height images were taken under the non-resonant PeakForce feedback control (Bruker, USA) using SCANASYST-AIR-HR cantilevers with a spring constant of 0.5 - 0.8 N/m (Bruker, CA, USA), facilitating a higher imaging resolution (~ three times) compared to that obtained with Nanoscope Multimode III. All the data was collected with the tapping mode, which allows high-quality imaging without sample damage. Four individual overlapping images along the fibre length (16 μm × 4 μm) were collected and stitched together. The obtained images were processed using the Nanoscope Analysis 1.7 software. Plane and flatten functions were applied to account for any tilt due to the fibre cylindrical geometry; contrast/brightness alterations and false-colouration were applied to emphasise the inhomogeneous nature of the fibre surfaces. Schematic representation of AFM set-up can be found in Supporting Materials SM.01.

X-ray diffraction (XRD) For the XRD measurement at the beamline BM28, European Synchrotron Radiation Facility (ESRF), a sample of vertically aligned fibres was fixed between two pieces of Kapton (poly (4,4'-oxydiphenylene-pyromellitimide) tape. An X-ray beam with an energy of 14 keV and a corresponding wavelength λ = 0.886 Å was used. XRD scans were performed in the transmission mode, with a 0.24 m sample-to-detector distance and using a MAR165 detector. Calibration was performed using aluminium behenate ($C_{66}H_{129}AlO_6$) and zinc oxide (ZnO) powder standards. The diffraction images were processed using *pyFAI*, a pythonic library for 1D azimuthal / 2D radial integrations of diffraction images [46]. The analysis was performed in IGOR Pro (WaveMetrics, Portland, USA) and the peaks were assigned based on the available literature. XRD patterns on polyolefins are often reported as scattered intensity *vs.* diffraction angle (2θ) [47-49], and here we will plot the intensity *vs. q*, where the momentum transfer $q = 4\pi \sin\theta / \lambda$. Combined with the Bragg law $2d \sin\theta = n\lambda$ the *d*-spacing of the fibre crystal could be determined as from the n^{th} Bragg peak position q_n as $d = \frac{2n\pi}{q_n}$.

Results and discussion

Water contact angles on the fibres were successfully obtained using the spray-method developed, which produced droplets with a volume of 0.020 – 0.034 μL. Table 1 shows fibre wettability results. As expected, all the polyolefin fibres were hydrophobic with an average static contact angle of 114-126°. We note that Schellbach *et al.* [50] have developed a novel method in which contact angles were calculated indirectly from the analysis of the dimensions of spherical menisci of a liquid column formed between two fibres aligned parallel to each other in proximity (~ mm). The method required spreading of the liquid droplet on the fibres, and was thus suited for the hydrophilic natural fibres they tested (*e.g.* CA 20-70^o). Our sessile

drop spray-on method seemed well suited for direct measurement on hydrophobic fibres using multiple drops without any delicate fibre alignment, analogous to the classic contact angle measurement on a flat substrate. To our knowledge, such *static* contact angle values have not been previously reported for single microfibres. The contact angle values obtained here are higher than those reported for the *dynamic* water contact angles of untreated PP (91°) [51] and PE (90°) [52] single fibres. It should be stressed that less hydrophobic surfaces could potentially result in an axisymmetrical or a clamshell droplet configuration, making the determination of contact angles more difficult [53-55].

Optical images in Figure 3a-d reveal different waviness or crimp along the fibre length in samples 1-4. Fibres in samples 2 and 4 are of a planar crimp configuration, and their corresponding fabrics 1 and 3 show superior cohesion, web loftiness, and tactile properties. The crimp frequency (C_f) and crimp degree (K_g) for samples 1-4, calculated according to China National Standard 14338-2008 [56], are listed in Table 1. For samples 1 and 2 K_g = 9.6, whilst K_g = 14.1 for samples 3 and 4, with corresponding fibre diameter d_f =18.4 μm and 16.9 μm, respectively. This suggests that, as the fibre gets thicker and more rigid, the crimp degree is reduced (Table 1).The crimp in single fibres caused numerous voids between the fibres in nonwoven fabrics (samples 1 and 3) which can improve air permeability, when the nonwoven fabric is made from fibres of a circular cross-section, as in this study [57].

Monocomponent fibres (sample 5 and 6) appeared non-crimped (Figure 3e-f), consistent with spunbonding manufacturing process in which straight, continuous fibres are produced. Such a process combines fibre spinning followed by the web formation, in contrast to traditional processing in which fibres are first spun, then collected and finally converted into webs [58]. The presence of crimps in samples 2 and 4 may imply that fabrics made of those fibres are of superior softness in comparison to non-crimped polypropylene samples 5 and 6. However,

spunbonded nonwovens made of monocomponent PP fibres are known to possess great tensile strengths, abrasion resistance, and elastic properties, which along with their tactile properties can be controlled with thermal calender bonding process conditions (e.g. temperature and pressure) in order to obtain equally important optimal strength and softness [59].

The fibre diameters d_f of all the samples, determined with SEM as listed in Table 1, were all below 20 μm with small variations within the same batch, indicating good manufacturing reproducibility. SEM images of the cross-section of the bicomponent samples show that they were approximately circular with a core-sheath structure, exemplified in Figure 4a and b for samples 2 and 4, respectively, with that of the core and the sheath accounting for 60% and 40% of the total diameter on average, respectively. All the studied samples were of circular geometry (*cf.* SM.02), and such circular fibres are known to facilitate the highest air permeability in nonwovens [60].

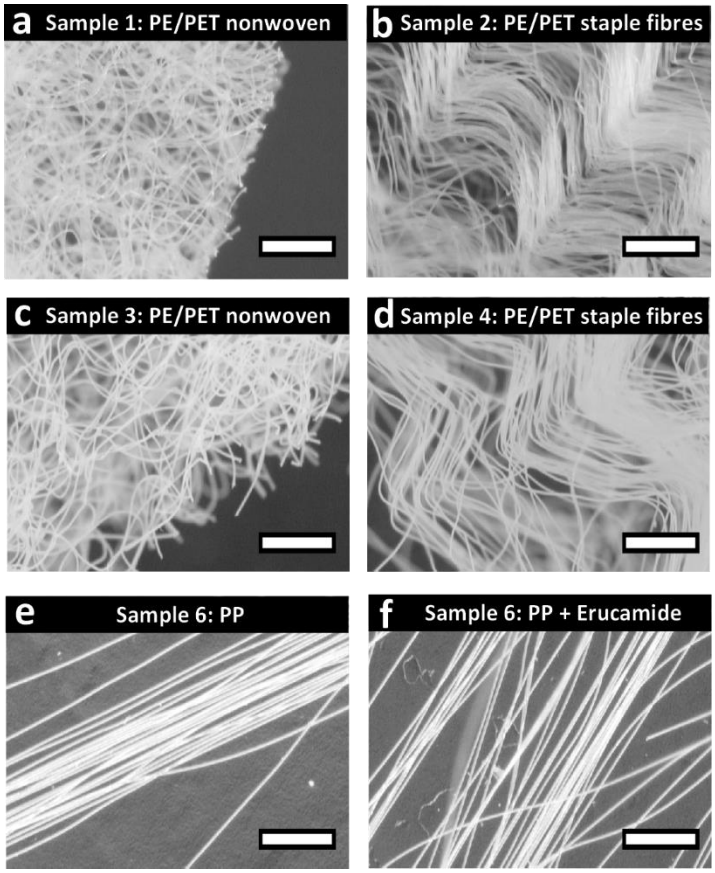

Figure 3 Optical microscopy images of samples 1-6 in (a) - (f), respectively. All the scale bars represent 500 μm.

In addition, both the fibre composition and the manufacturing process appear to influence fibre morphology. Example SEM images in Figure 4 highlight common topographic features found on the fibres. Numerous cross-links were found between the fibres entangled in nonwoven samples 1 and 3 (Figure 4c-d). This could be due to the thermal bonding process (through-air bonding) used as a part of nonwoven-making process, allowing the PE sheath to melt to create bonding points with adjacent fibres. Furthermore, for some of the fibres removed from nonwoven samples 1 and 3, the sheath peeled off the core (Figure 4e). Such peeling-off was not observed in samples 2 and 4; instead, the core was enveloped by the sheath (Figure 4f). This shows that the elevated temperature used in the nonwoven fabric production (samples 1

and 3) affected/weakened the adhesion at the interface between coextruded polymers (*i.e.* the core and sheath) [61].

Furthermore, nonwoven-making process conditions were found to influence the fibre morphology. For PE/PET staple fibres, microfibrillar structures with long-range linear features were found oriented along the fibre length (samples 2 and 4; Figure 4i and j); whereas for nonwoven fibres microporous structures were observed, with the typical pore diameter of *ca.* 0.2-0.3 μm (samples 1 and 3; Figure 4g and h). Such fibre porosity could originate from a thermal phase separation between the solvent and the polymer phase after cooling of the polymer/solvent mixture [62]. Similar morphology was found in linear low-density PE microfibres produced with a high-temperature electrospinning process from p-xylene solution [63], as well as in poly(propylenecarbonate)/poly(3-caprolactone) nanofibers electrospun from a dichloromethane solution [64]. Both the porosity and the fibrillar texture may affect fibre wettability and mechanical properties, in addition to playing a key part in inter-fibre frictional interactions, which is essential for fibre mutual support and resistance to buckling under compression [65, 66].

For monofilament samples, sample 5 possessed a neat and smooth topography with sparse rounder features (Figure 4k and l), whereas numerous branched clusters of a random distribution were found on the surface of sample 6 (Figure 4m and n) attributed to erucamide aggregates migrated to the PP fibre surface. More examples of the above described topographic details for sample 1-6 can be found in Supporting Materials SM.02.

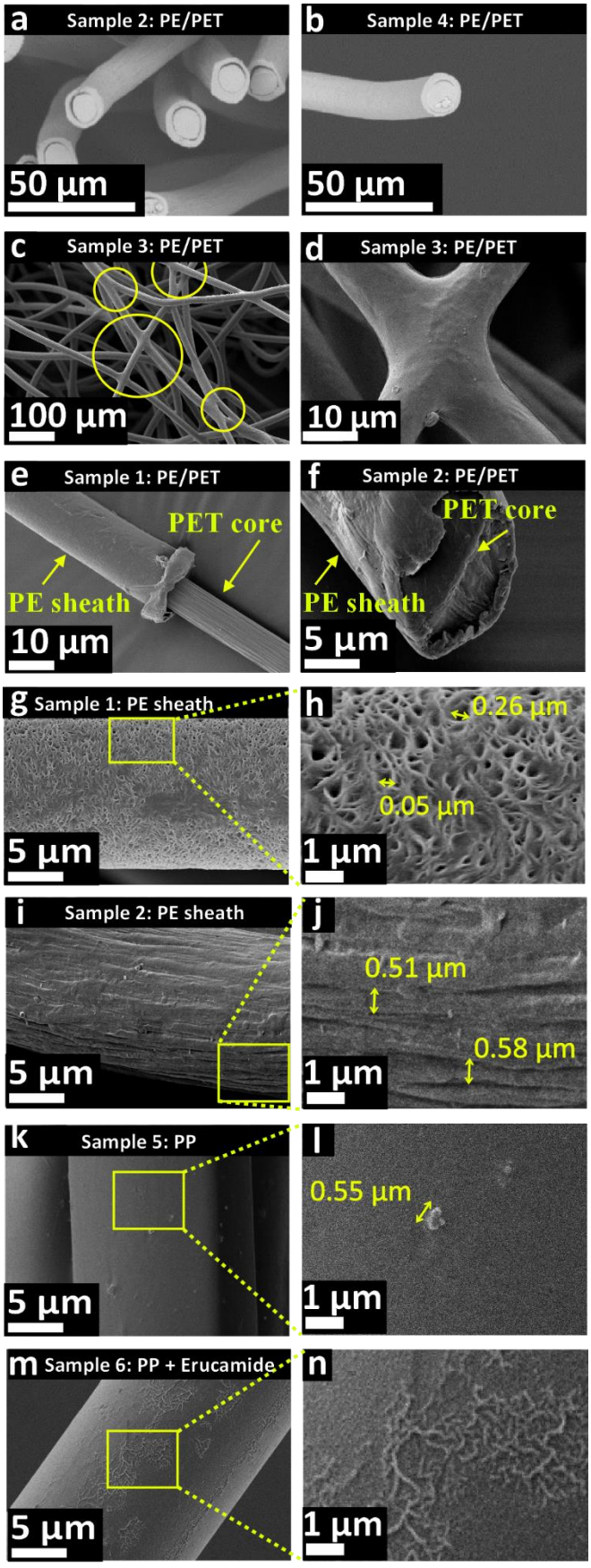
a
Sample 2: PE/PET
50 µm
b
Sample 4: PE/PET
50 µm
c
Sample 3: PE/PET
100 µm
d
Sample 3: PE/PET
10 µm
e
Sample 1: PE/PET
PET core
PE sheath
10 µm
f
Sample 2: PE/PET
PET core
PE sheath
5 µm
g
Sample 1: PE sheath
5 µm
h
0.26 µm
0.05 µm
1 µm
i
Sample 2: PE sheath
5 µm
j
0.51 µm
0.58 µm
1 µm
k
Sample 5: PP
5 µm
l
0.55 µm
1 µm
m
Sample 6: PP + Erucamide
5 µm
n
1 µm

Figure 4 SEM images showing fibre morphology and topography: (a-b) Cross-section of bicomponent PE/PET staple fibres of sample 2 (PE/PET staple fibres) and sample 4, respectively (also representative for sample 1 and 3; images not shown); (c-d) Fibres cross-linked in nonwoven sample 3 (with the images for sample 1 shown in SM.02); (e) PE sheath peeling off PET core in sample 1 (image for sample 3 in SM.02); (f) PET core enveloped by PE sheath in sample 2 (image for sample 4 in SM.02); (g) porous surface of nonwoven sample 1 (image for sample 3 in SM.02); (h) enlarged view showing numerous pores of the rectangle region in (g); (i) microfibrillar surface of sample 2 (image for sample 4 in SM.02); (j) enlarged view showing microfibrils of the rectangle region in (i); (k) surface of sample 5; (l) enlarged view showing the neat surface with rare rounder features of the rectangle region in (k); (m) surface of sample 6; and (n) enlarged view showing branched clusters of the rectangle region in (m).

AFM imaging provided complementary nanoscale visualisation of the fibre surface, also allowing average surface roughness to be calculated. Typical AFM topography images of the fibres with the corresponding roughness profiles along the fibre length are presented in Figure 5. For nonwoven samples 1 and 3 (which exhibited PE sheath peeling off), the PET core of the fibre was also imaged (Figure 5a2 and c2). The AFM images confirmed the porous structure of the PE sheath of samples 1 and 3, with the depth of the pores in the range of a few to 100 nm (Figure 5a1 and c1). On the other hand, the fibrillar structures were observed on the single fibre of sample 2 and 4 (Figure 5b and d, respectively) as well as on the PET core of nonwoven samples 1 and 3 (Figure 5a2 and c2), with the fibril width in the rage of a few hundred nm to up to 1 μm. In addition, on sample 4, multiple ridges of height up to 200 nm were found next to the microfibrils, manifesting in a bumpy, rigid surface (Figure 5d). Further detailed discussions on the effect of nonwoven making process on fibre topography along with the corresponding surface roughness profiles can be found in SM.03.

For the monofilament fibres from sample 5, its topography appeared smooth, with sparsely distributed larger surface structures of up to 200 nm in height (Figure 5e). Given that the fibre from sample 5 consisted of pure PP, we suggest that these surface textures were physical features possibly resulting from fibre processing. In contrast, the sample 6 fibre was found to be coated with a relatively large number of surface structures of a few nm to a few hundred nm in height, attributed to erucamide migration to polymer surface in the "blooming" process (Figure 5f). These AFM results are consistent with our SEM study of the fibre surface topography (Figure 6). Different appearances of erucamide in sample 6 registered as branched clusters in the SEM image and as islands of crystals in the AFM image reflect the uneven distribution of erucamide and the morphological variations of its surface aggregates on PP. Additional SEM and AFM images further illustrate such variations (SM.04).

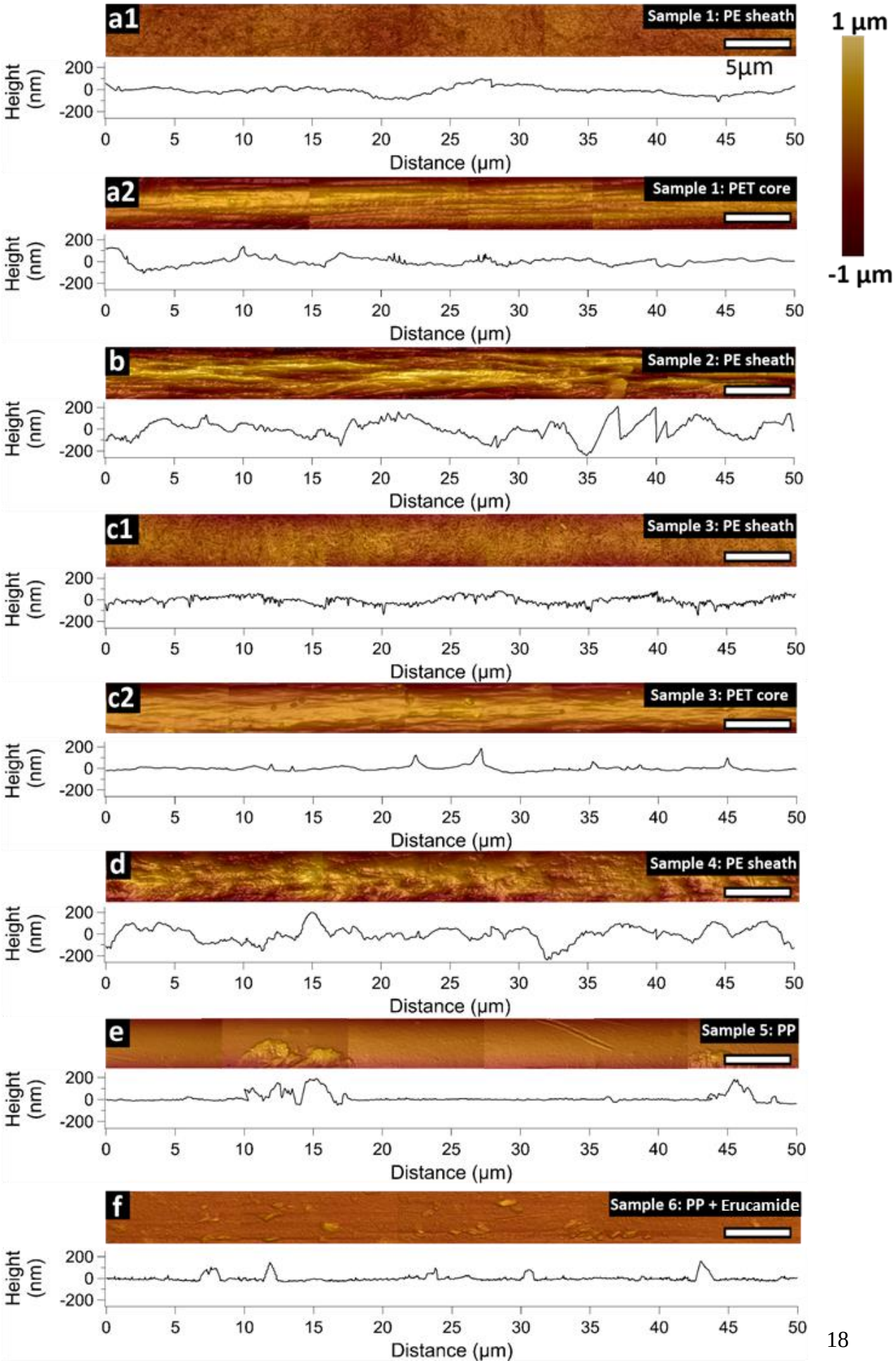
a1
Sample 1: PE sheath
5µm
1 µm
-1 µm
Height (nm)
200
0
-200
0 5 10 15 20 25 30 35 40 45 50
Distance (µm)
a2
Sample 1: PET core
b
Sample 2: PE sheath
c1
Sample 3: PE sheath
c2
Sample 3: PET core
d
Sample 4: PE sheath
e
Sample 5: PP
f
Sample 6: PP + Erucamide

Figure 5 AFM images (50 μm in length × 4 μm in width) with corresponding roughness profiles along the fibre length: (a1) Sample 1 sheath; (a2) sample 1 core; (b) sample 2; (c1) sample 3 sheath; (c2) sample 3 core; (d) sample 4; (e) sample 5; and (f) sample 6. The scale bar in (a1) represents 5 μm and is applicable to all the images.

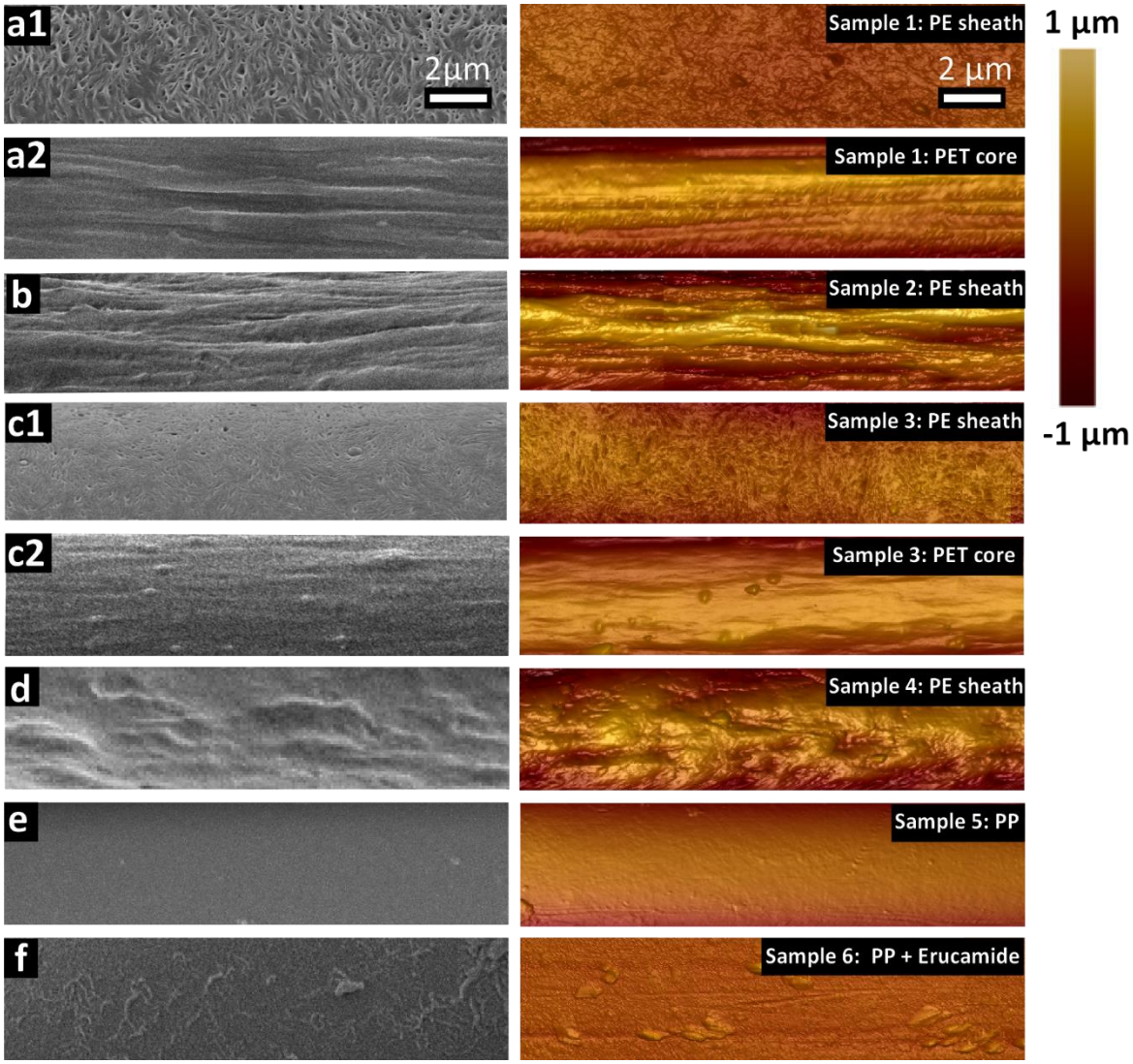

Figure 6 Comparison between SEM (left column) and AFM (right column) images of (a1) sample 1 sheath; (a2) sample 1 core; (b) sample 2; (c1) sample 3 sheath; (c2) sample 3 core; (d) sample 4; (e) sample 5; and (f) sample 6. The scale bar in (a1) represents 2 μm and is applicable to all the images.

The fibre surface roughness is one of the key parameters affecting fibre tactile properties, as different surface roughness leads to different actual contact areas and friction during fibre contact with the skin or other fibres. From the AFM images (50 μm in length and 4 μm in width; Figure 5), the arithmetic mean of roughness (R_a), the maximum roughness (R_{max}), and the root mean square roughness (RMS, R_q) were evaluated, averaging from the images (cf. Table 2 and Figure 7). The mathematical definition of obtained roughness parameters can be found in SM.03. The error bars for each of the roughness parameters (R_a, RMS, and R_{max}) were determined as the standard deviation of the results obtained from the four images combined to show the topography along fibre length (16 μm × 4 μm) (Figure 5). All the calculated roughness parameters follow a similar trend, showing that both fibre entanglement in the nonwoven making process and the slip additive (erucamide) treatment decreased their surface roughness, an effect more pronounced for the PE/PET than the PP fibres. We note that the topography images of sample 5 indicate a lower value of the surface roughness in comparison to sample 6 (Figure 5e and f). The presence of a few large lamellae on the PP surface of sample 5 (Figure 5e) caused a significant *standard deviation* (SD in R_a ~ 13 nm and SD in RMS ~ 21 nm), in contrast to sample 6 (Figure 5f) (SD in R_a ~ 1 nm and SD in RMS ~ 2 nm). This resulted in their apparently similar roughness values.

Table 2 Average surface roughness.

Sample no.	**R_a (nm)**	**RMS (R_q) (nm)**	**R_{max} (nm)**
1 PE sheath	27 ± 7	33 ± 7	230 ± 30
1 PET core	30 ± 4	39 ± 6	343 ± 78
2 PE sheath	70 ± 6	90 ± 9	711 ± 87
3 PE sheath	31 ± 4	39 ± 5	347 ± 88
3 PET core	20 ± 4	30 ± 8	346 ± 155

4 PE sheath	51 ± 11	64 ± 12	451 ± 46
5 PP	15 ± 13	23 ± 21	258 ± 154
6 PP + Erucamide	14 ± 1	23 ± 2	297 ± 21

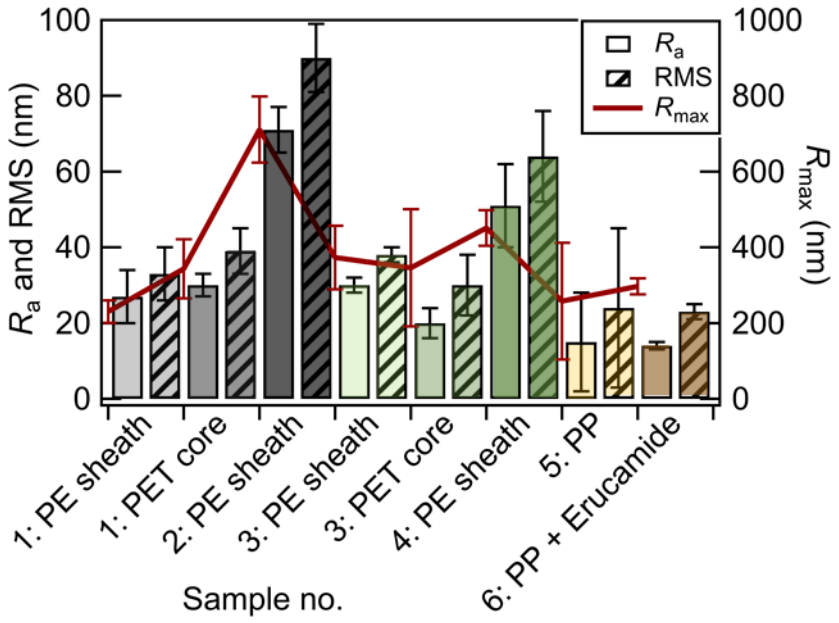

Figure 7 Surface roughness parameters averaged over all the studied samples: arithmetic average of the absolute values of the surface height deviations measured from the mean plane (R_a), the root mean square average of height deviations (RMS), and the maximum vertical distance between the highest and lowest data points in the image following the planefit (R_{max}).

XRD measurements were performed on sample 5 and 6 (PP fibres without and with erucamide, respectively). As shown in Figure 8, the XRD patterns for both samples consist of crystalline Bragg peaks and also broad peaks at q = 5-30 nm^{-1}, showing their semi-crystalline structure, characteristic for polymeric materials [67]. The 2D diffraction patterns show four slightly diffuse rings with some discontinuities. The 1D line plots for these two samples show almost identical peaks at q = 9.9 nm^{-1} (d = 6.32 Å), q = 11.9 nm^{-1} (d = 5.28 Å), q = 13.1 nm^{-1} (d = 4.80 Å), and q = 15 nm^{-1} (d = 4.19 Å), corresponding to the (110), (040), (130) and (111) crystal

planes, and the low intensity peaks at q = 18.0 nm^{-1} (d = 3.49 Å), q = 19.1 nm^{-1} (d = 3.29 Å), and q = 20 nm^{-1} (d = 3.14 Å) correspond to the (060), (200) and (220) crystal planes. These peaks and the corresponding d-spacing are characteristic of isotactic α-propylene[47-49]. As such, the XRD measurements did not detect the presence of any erucamide on sample 6 (revealed by AFM imaging) which might result from the very small amount of erucamide additives in the fibre formulation. This demonstrates the sensitivity of the AFM imaging which allowed us to observe that the presence of erucamide on the fibre surface. A nano-focused XRD study with a higher spatial resolution is underway to determine the distribution of erucamide in the fibre, which will allow the effect of erucamide concentration and the nonwoven making process on the fibre crystal structure to be further evaluated.

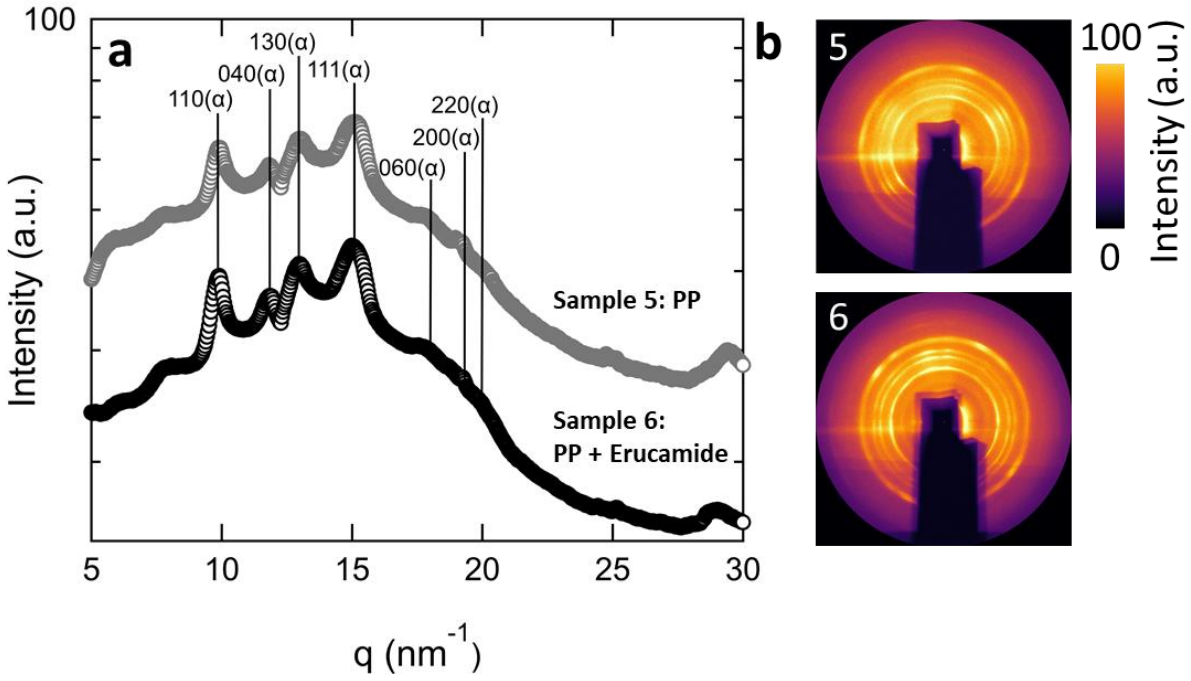

Figure 8 (a) Integrated XRD curves and (b) their corresponding 2D diffraction patterns (area detector images) of sample 5 and 6.

The surface structure of samples 5 and 6 (*cf.* Table 1) was examined more closely on a nanoscale with the topographic imaging, allowing for a comparison between surface

roughness parameters (R_a, RMS, and R_{max}) calculated based of the topography images in Figure 9a and d of the neat PP surface of sample 5 (Figure 9a-c) and the sample 6 with its surface enriched with the slip additive erucamide (Figure 9d-f). Amorphous regions with a few small rounder features up to 15 nm in height were found in a 4 μm × 4 μm area of sample 5, leading to R_a, RMS, R_{max} of 2 nm, 3nm and 51 nm, respectively, indicating a neat, undisturbed PP surface (Figure 9a-c). In contrast, sample 6 was covered densely with multi-layered plate-like crystals of hundreds of nm in height (Figure 9d-f), in contrast to the underlying PP surface with small circular lamellae (dashed square in Figure 9d). The presence of numerous nanostructures caused the surface roughness to be a factor of 10 higher than that of sample 5, with R_a, RMS, and R_{max} of 72 nm, 85 nm and 525 nm, respectively. The observed structures are consistent with those observed by Ramirez in a study on erucamide and behenamide in linear low-density PP films [26]. One would expect that the non-uniform slip additive distribution could affect fibre frictional properties; however, it was shown that the full additive surface coverage was not crucial to obtain the minimum coefficient of friction (CoF) [21]. Indeed, it has been suggested that the frictional properties of nanotextured surfaces are intricately dependent on the geometry, local slope, and distribution of the surface texture, with modifications of classic Amontons' laws of friction proposed to account for the presence of surface nanostructures [68-70]. The roughness profile of 30 erucamide layered structures present on the fibre surface with an area of 16 μm^2 has been obtained (Figure S8 in SM.03). The studied discrete crystal domains varied in size and height, with the majority between 200 and 300 nm in the lateral size and smaller than 20 nm in height. The thinnest layer measured with AFM was 4 ± 1 nm thick, which is consistent with the theoretical value calculated for an erucamide bilayer [71]. Such a layered assembly of erucamide is justified by its chemical structure: the presence of the amide headgroups results in a bilayer of hydrogen-bonded erucamide molecules, leading to the eventual erucamide multilayer formation (Figure 10) [71, 72].

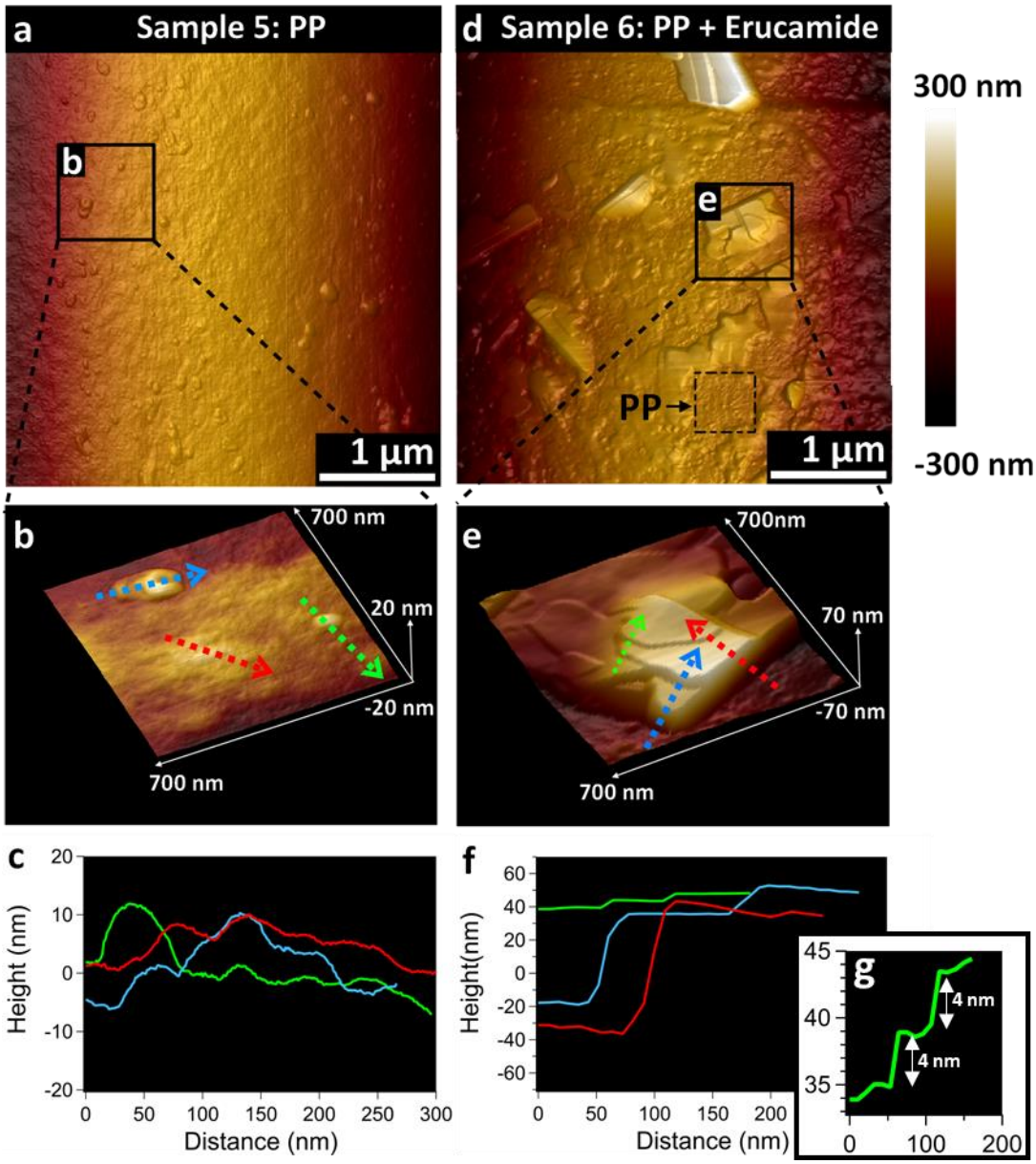

Figure 9 AFM images of sample 5 (a-c) and 6 (d-f): (a) 2D height image of sample 5; (b) enlarged view showing a 3D height image of the square region labelled (b) in (a); (c) surface line profiles corresponding to the lines in (b) on sample 5; (d) 2D height image of sample 6 covered with multi-layered erucamide aggregates (*e.g.* the square region labelled (e)) on top of PP regions (*e.g.* the dashed square); (e) enlarged view showing a 3D height image of the square region labelled (e) in (d), highlighting a multi-layered erucamide crystal structure on sample 6;

and (f) surface line profiles corresponding to lines in (e) on sample 6; (g) line profile along the green dashed arrow in (e) showing 4 nm steps in the erucamide multilayer.

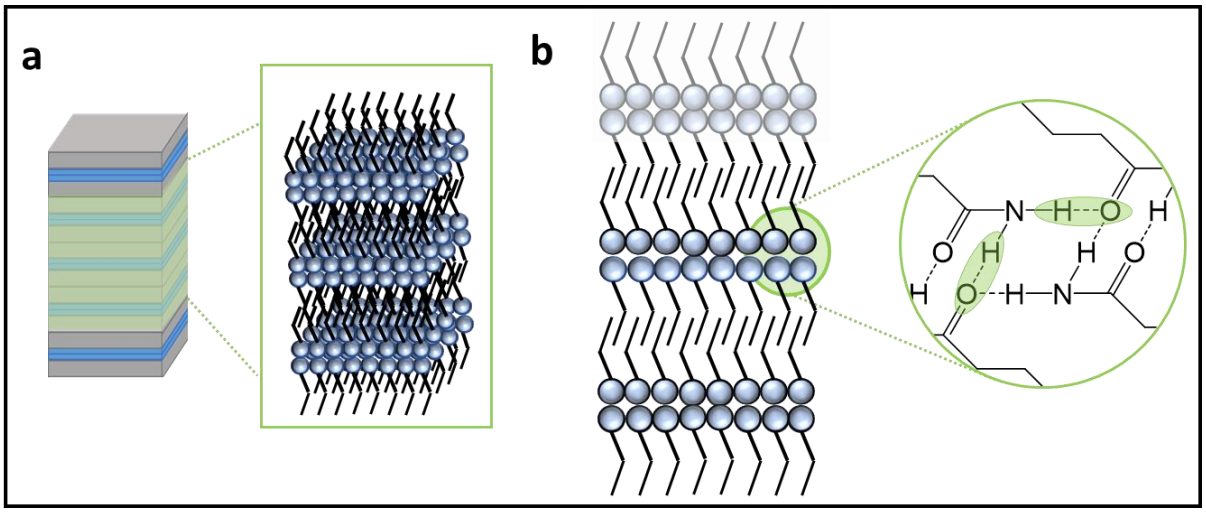

Figure 10 (a) Schematic representation of erucamide crystals with multilamellar structure; (b) 2D cross-section of multilayer of hydrogen-bonded erucamide molecules.

The influence of fibre morphology on their nanomechanical properties was studied by Peak Force QNM mapping. During AFM scans, the tip could become gradually contaminated with the sample, thus affecting the adhesion force value obtained. A new AFM cantilever was thus used for each sample, and the obtained adhesion value was also normalised with respect to the adhesive force on a mica surface, allowing for a comparison between samples 1-6 [73-76]. The data used for normalisation with mica was used only where the tip was in a comparable state, i.e. the data before the first discontinuity was normalised with the calibration measurement made on mica before the tip was used on the fibre, whereas the data between the last discontinuity and the end of the scan was normalised with the calibration measurement taken on mica with the same tip after scanning the fibre. In this way, it was assured that the tip was in the same state on the mica and the fibre for the relevant data, which allowed for an internally consistent comparison between samples where the tip condition may change during imaging and affect the absolute values of the measured adhesive force. The error bars for each of the

adhesive response $\overline{F_a}$ of the AFM probe against all the samples were determined as the root mean square (RMS) average of the adhesive force deviations from the adhesion map, normalised by the adhesive response of AFM-tip towards the mica surface. In general, the relative adhesive responses differed between the fibres depending on their processing and surface treatment. Figure 11a shows the differences in such normalised adhesive forces $\overline{F_a}$. For nonwoven samples 1 and 3, the difference in the morphology of the fibre porous PE sheath and the microfibrillar PET core significantly affected the adhesion responses. That is, the value for the PET core (sample 1: $\overline{F_a}$ = 1.13 ± 0.38; sample 3: $\overline{F_a}$ = 1.02 ± 0.61) was twice that for the PE sheath (sample 1: $\overline{F_a}$ = 0.64 ± 0.44, sample 3: $\overline{F_a}$ = 0.42 ± 0.15). For both single fibre samples 2 and 4, the value for the microfibrillar PE sheath was higher than that for the nonwoven sample 1 and 3 porous surfaces. The slip additive treatment of sample 6 led to a decrease in the probe-surface adhesion ($\overline{F_a}$ = 0.61 ± 0.3) from $\overline{F_a}$ = 1.09 ± 0.23 for sample 5, indicating that the presence of erucamide significantly affected PP surface adhesion properties and thus its efficacy to tailor fibre tactile properties. The height and adhesion images of samples 1-6 are collated in Figure S10 in SM.05.

Comparison between height (Figure 11b, d1-d2) and adhesion (Figure 11c1-c2) images from a single fibre of sample 3 allowed us to correlate the fibre morphology features with its adhesion properties. Comparison of height and adhesion maps of the PET core of samples 1 and 3 shows that more elevated regions exhibited lower adhesion (SM.05). Raw adhesive response (F_a) of the PE sheath of nonwoven samples 1 and 3 was up to 12 nN higher inside the pores than for the surrounding area (Figure 11c2 and d2). This is likely caused by the greater contact area between the AFM probe and voids present on the fibre surface. No correlation between the adhesion and height was found for samples 2 and 4.

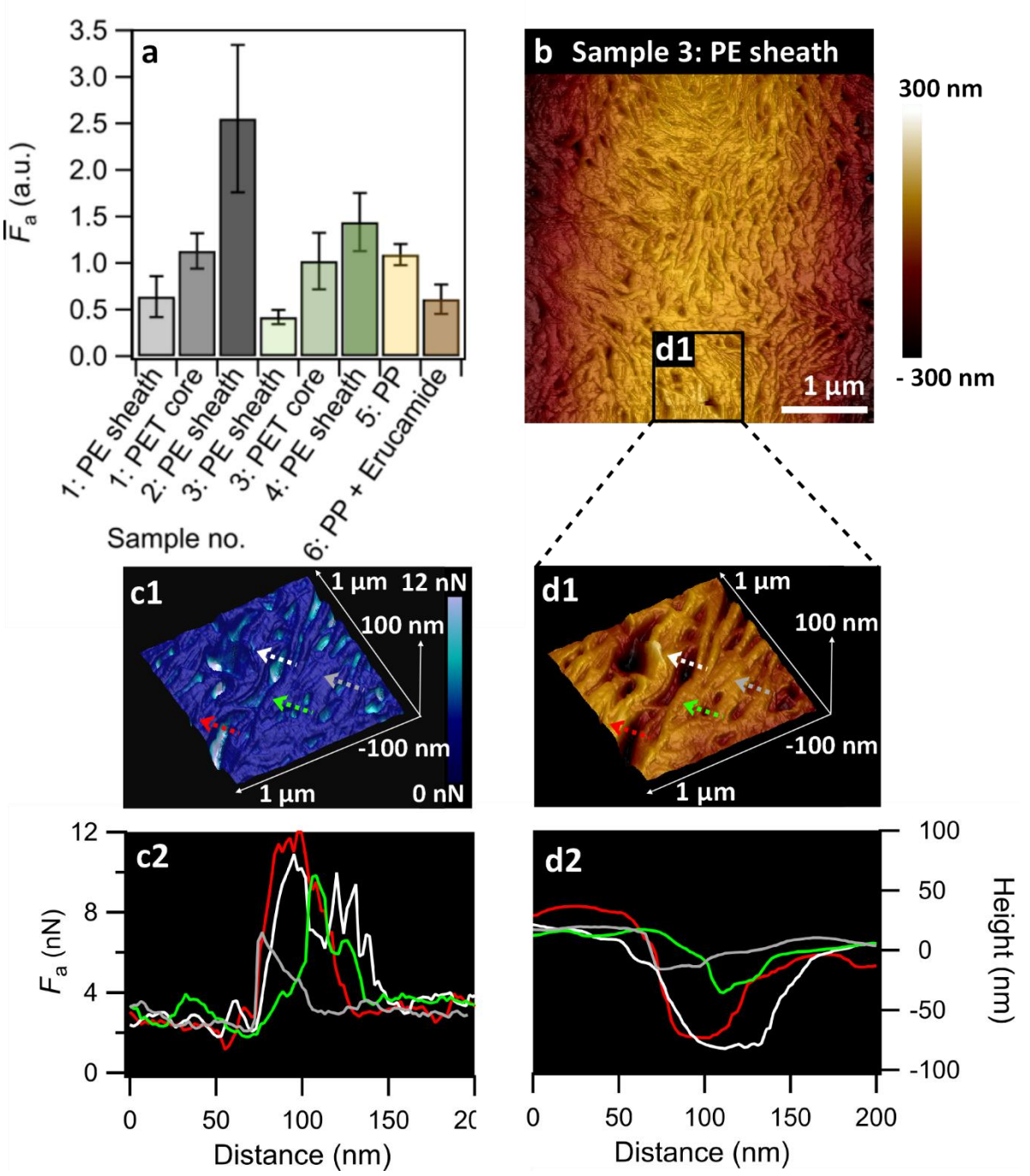

Figure 11 (a) Normalised adhesive response $\overline{F_a}$ of the AFM probe against all the samples; (b) 2D AFM height image of the porous PE sheath for sample 3; (c1) 3D AFM adhesion image and (c2) raw adhesion force F_a profile for sample 3 (corresponding to lines in c1); (d1) enlarged view showing a 3D height image of the square region labelled (d1) in (b) and (d2) line profile for sample 3 (corresponding to lines in d1).

Figure 12 correlates the height (Figure 12a) and adhesion (Figure 12b) maps of the erucamide crystals and the polypropylene surface. The value of the raw adhesion force F_a exhibited by the AFM tip was lower for approximately 0.5 nN on erucamide than on surrounding amorphous propylene (Figure 12c and d). Since polypropylene is a nonpolar polyolefin while erucamide consists of both a nonpolar tail and a polar primary amide headgroup, the fibre chemical surface structure can be verified by the contact angle measurement. The surface treated with erucamide was found to remain hydrophobic with only a small decrease detected in the water contact angle from θ = 126.3 ° ± 0.4 ° (sample 5) to θ = 122.4° ± 0.3° (sample 6) (Table 1). This suggests that the erucamide multilayers detected by AFM were densely packed on the fibre surface, with the hydrophobic tails oriented outwards [77]. A similar conclusion was drawn in Dulal *et al.*'s work on erucamide performance in high-density polyethylene closures [32]. Other studies suggested that the hydrophilic groups of the slip additives were exposed to the air, whilst the hydrophobic chains stayed embedded within the polymer, resulting in decrease of water contact angle from 104° (low density PE) to 94° within short period of time (40 min) during erucamide migration to the polymer film surface [30]. As stated by Dulal *et al.,* such result may be a consequence of short migration time frame, insufficient for the migration of erucamide molecules on the polymer surface to form multilayers as in our case study. Our analysis shows that he adhesion on the erucamide crystals appeared to depend on the local curvature, with a higher value on the side and the bottom of the crystal ridges than for its top (SM.05 Figure S12). Such observation is consistent with a higher adhesive response between the silicon AFM tip and the exposed erucamide headgroups at the edges of the multilamellar structure. Alternatively, a greater adhesive response could also result from a greater area of contact while scanning the side or bottom of the erucamide layer with the crystal surface wrapping around the tip, than the area of contact between the probe tip and the top of the crystal [78]. Additional examples of erucamide affecting PP fibre adhesion to decrease can be found

in Supporting Materials SM.05 Figure S10. An X-ray reflectivity study is underway to better understand the assembly of erucamide on polymer fibres.

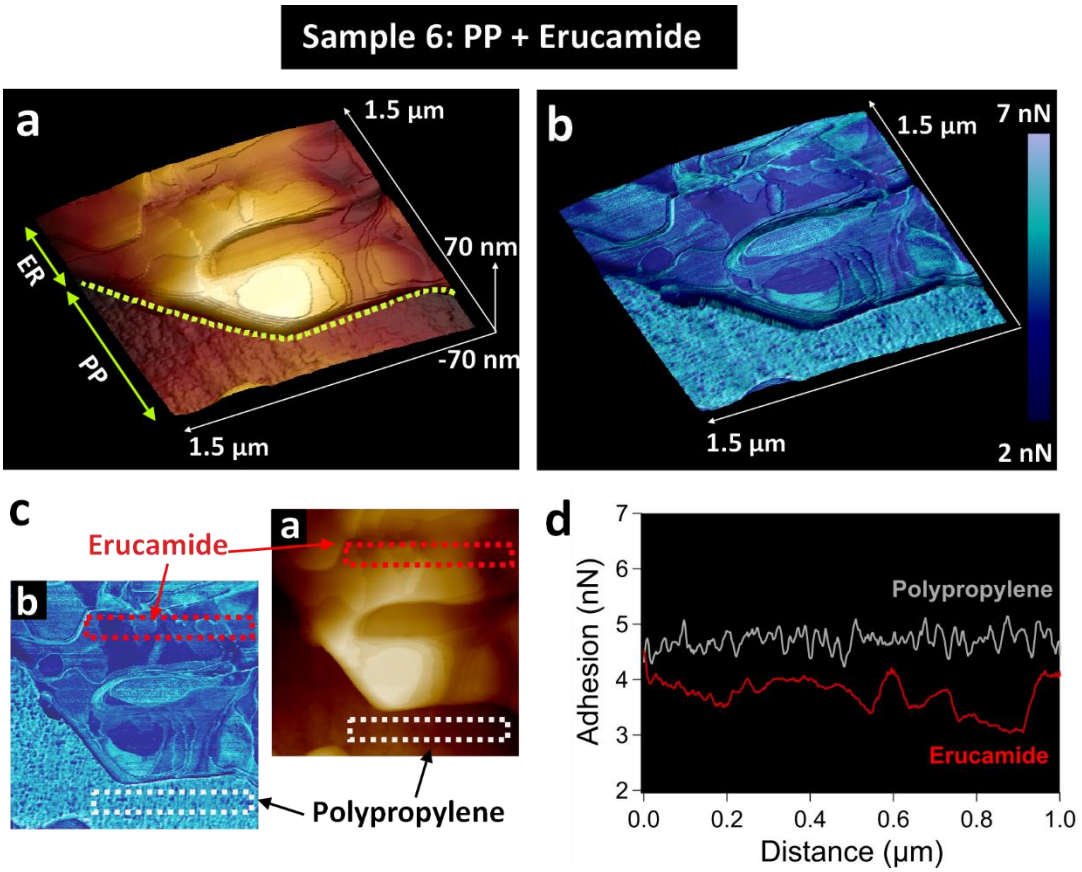

Figure 12 (a) 3D height image with marked areas of erucamide (ER) and PP; (b) 3D adhesion image; (c) 2D adhesion and height maps with marked areas of erucamide (red dotted rectangle) and PP (grey dotted rectangle), and (d) raw adhesion force F_a profiles corresponding to the regions in (c). All for sample 6, i.e. PP with erucamide additives.

Conclusions

Fibre geometry, surface structure, wettability and nanomechanical properties rely on and can be tuned by fibre composition and manufacturing. Understanding the effect of fibre processing on these fibre properties is important for optimisation of manufacturing fibrous materials with desired properties.

It has been generally considered a challenging task to assess wettability of synthetic microfibre. The "spray-on" method with custom-designed fibre holder here allowed for a direct measurement of static contact angles of water droplets on the fibres. It was demonstrated that the surfaces of all the six polyolefin fibres studied were hydrophobic. SEM together AFM imaging revealed the morphological details of single fibres, allowing a correlation between the manufacturing process and the observed fibre surface structure, showing a significant effect imparted by the thermal through-air bonding process of the bicomponent PE/PET fibres, causing fibre topographical features to change from being microfibrillar to being porous. Overlapping plate-like structures of 4 ± 1 nm layers found on the PP fibre can be attributed to erucamide bilayers, the slip additive, migrated onto the fibre surface. This caused the fibre topography to significantly differ from the flat, neat surface of fibre composed of pure PP without any additives, albeit XRD study did not imply erucamide affecting fibre crystal structure. We observed that both the nonwoven making process and the slip additive treatment affected the fibre surface roughness and their nanomechanical properties. Correlation of fibre topography with nanomechanical properties gained through adhesion force mapping showed potential for control and manipulation of fibre nanomechanical properties through implementation of the through-air thermal bonding process as well as the slip additive treatment during fibre manufacturing. Both processes could lead to significant modifications of the fibre topography, affecting fibre adhesive properties. For instance, the through-air bonding process could impart changes in the fibre surface morphology, transforming it from being microfibrillar to less adhesive, porous surface structures; the presence of erucamide on the fibre surface could also reduce the tip-fibre adhesion when compared to the neat fibre, pointing to the potential of both processes to tune fibre tactile properties.

Previously, the porosity in nonwoven fabrics has been generally referred to as “numerous air gaps between the fibres bonded in a web matrix, leading to a superior air permeability of the material” [79, 80]. Here, we have observed directly such porous surface on single fibres as a result of through-air bonding process. Furthermore, the efficacy of erucamide as a slip additive to modify frictional properties has been previously demonstrated on macroscopically flat surfaces [21, 81]. Here, we have provided the direct evidence and detailed structural details of erucamide nanocrystals on the surface of cylindrical microfibres, imparting significant modifications to the adhesive properties of the fibres, alluding to their roles in tailoring tactile properties of synthetic microfibres highly desired in personal care products. The wettability, surface morphology, and adhesion properties from this study, obtained with unprecedented resolution and details on single fibres, are valuable to informing rational design of fibre processing such as through-air bonding and slip additive treatment for fibre optimal properties, critically important in many industrial applications.

A nano-focused XRD study is currently underway to determine the distribution of erucamide across the fibre length and width, in order to investigate the effect of erucamide concentration and nonwoven making process on the fibre crystal structure. In addition, an X-ray reflectivity study is in progress to better understand the self-assembled structure of erucamide on surfaces and the underlying mechanism for its effect on fibre nanomechanical properties.

Acknowledgements

D.G. is supported by the UK Engineering and Physical Sciences Research Council (EPSRC) and Procter and Gamble Industrial Case Award. P.W. was supported by the Bristol Centre for Functional Nanomaterials (BCFN, EPSRC grant no. EP/G036780/1). W.H.B. would like to acknowledge funding from the EPSRC (EP/H034862/1), European Cooperation in Science and

Technology (CMST COST) Action CM1101 “Colloidal Aspects of Nanoscience for Innovative Processes and Materials”, and Marie Curie Initial Training Network (MCITN) on “Soft, Small, and Smart: Design, Assembly, and Dynamics of Novel Nanoparticles for Novel Industrial Applications” (NanoS3; FP7 Grant No. 290251). We acknowledge the beamline BM28 at the European Synchrotron Radiation Facility (a UK EPSRC funded facility) for beam time (experiment no. SC-4401) and the staff there for their help during the experiment.

References

1. Ejima, S., *et al*., 1972, *Method of forming autogenously bonded non-woven fabric comprising bi-component fibers, US4189338A*.
2. Kobayashi, Y., *et al*., 1986, *Very soft polyolefin spunbonded nonwoven fabric, US4810556A*.
3. Pike, R.D., *et al.*, 1992, *Nonwoven multicomponent polymeric fabric and method for making same, US5382400A*.
4. Pike, R.D., Peterson, R.M, 1994, *Nonwoven filter media for gas, US5597645A*
5. Brown, J.P., Stokes, T.J., 1995, *Protective cover fabric including nonwovens, US5662978A*.
6. Berrigan, M., *et al*., 2002 *Nonwoven amorphous Fibrous webs and methods for making them, US20030216099A1*.
7. Lalouch, L., *et al.*, 2010, *Nonwoven nanofiber webs containing chemically active particulates and methods of making and using same, WO2011133394A1*. 2010.
8. Seidel, D.L., *et al*., 2017, *Elastic nonwoven fibrous webs and methods of making and using, US9840794B2*. 2017.
9. Połowiński, S., *Deposition of polymer complex layers onto nonwoven textiles.* Journal of Applied Polymer Science, 2007. **103**(3): p. 1700-1705.
10. Xu, W. and X. Liu, *Surface modification of polyester fabric by corona discharge irradiation.* European Polymer Journal, 2003. **39**(1): p. 199-202.
11. Navaneetha Pandiyaraj, K., *et al.*, *Adhesive properties of polypropylene (PP) and polyethylene terephthalate (PET) film surfaces treated by DC glow discharge plasma.* Vacuum, 2008. **83**(2): p. 332-339.
12. Rietzler, B., T. Bechtold, and T. Pham, *Controlled surface modification of polyamide 6.6 fibres using CaCl2/H2O/EtOH solutions.* 2018. **10**.
13. Jaššo, M., *et al.*, *Grafting of maleic acid on the polyester fibres initiated by plasma at atmospheric pressure.* International Journal of Adhesion and Adhesives, 2006. **26**(4): p. 274-284.
14. Seto, F., *et al.*, *Surface modification of synthetic fiber nonwoven fabrics with poly(acrylic acid) chains prepared by corona discharge induced grafting.* Die Angewandte Makromolekulare Chemie, 1999. **266**(1): p. 56-62.
15. Kim, H. and J.-S. Bae, *Modification of polypropylene fibers by electron beam irradiation. I. Evaluation of dyeing properties using cationic dyes.* Fibers and Polymers, 2009. **10**(3): p. 320-324.

16. Wang, C.-C., *et al.*, *Surface modification of poly(lactic acid) fabrics with plasma pretreatment and chitosan/siloxane polyesters coating for color strength improvement.* Polymers, 2017. **9**(8): p. 371.
17. Radetić, M., *et al.*, *Antibacterial effect of silver nanoparticles deposited on corona-treated polyester and polyamide fabrics.* Polymers for Advanced Technologies, 2008. **19**(12): p. 1816-1821.
18. Markarian, J., *Slip and antiblock additives: surface medication for film and sheet.* Plastics, Additives and Compounding, 2007. **9**(6): p. 32-35.
19. DeLucia, M., *et al.*, *Methods of improving the softness of fibers and nonwoven webs and fibers and nonwoven webs having improved softness, US20040005457A1, 2003*.
20. Saleem, M., *et al.*, *Diffusion of organic penetrants through low density polyethylene (LDPE) films: Effect of size and shape of the penetrant molecules.* Journal of Applied Polymer Science, 1989. **37**(3): p. 617-625.
21. Ramirez, M.X., K.B. Walters, and D.E. Hirt, *Relationship between erucamide surface concentration and coefficient of friction of LLDPE film.* Journal of Vinyl and Additive Technology, 2005. **11**(1): p. 9-12.
22. Sharma, R., *et al.*, *SPE ANTEC™ Indianapolis, Impact of elevated temperatures on surface properties of erucamide-containing polyethylene films.* 2016: p. 627-631.
23. Briscoe, B.J., V. Mustafaev, and D. Tabor, *Lubrication of polythene by oleamide and stearamide.* Wear, 1972. **19**(4): p. 399-414.
24. Sharma, A.H. and B.C. Beard, *Mode of action of surface active slip and antiblocking additives.* Journal of Vinyl and Additive Technology, 1997. **3**(4): p. 309-313.
25. Burke, T.C., Gagne, J.D., 2002, *Controlled COF films, US7267862B1*.
26. Ramírez, M.X., D.E. Hirt, and L.L. Wright, *AFM Characterization of Surface Segregated Erucamide and Behenamide in Linear Low Density Polyethylene Film.* Nano Letters, 2002. **2**(1): p. 9-12.
27. Molnar, N.M., *Erucamide.* Journal of the American Oil Chemists' Society, 1974. **51**(3): p. 84-87.
28. Llop, C., *et al.*, *Control of the migration behavior of slip agents in polyolefin-based films.* Polymer Engineering & Science, 2011. **51**(9): p. 1763-1769.
29. Shuler, C.A., A.V. Janorkar, and D.E. Hirt, *Fate of erucamide in polyolefin films at elevated temperature.* Polymer Engineering & Science, 2004. **44**(12): p. 2247-2253.
30. Chen, J., *et al.*, *Fundamental study of erucamide used as a slip agent.* Journal of Vacuum Science & Technology 2007. **25**.
31. S. Rawls, A., *et al.*, *Evaluation of surface concentration of erucamide in LLDPE films*. Vol. 8. 2002. 130-138.
32. Dulal, N., *et al.*, *Slip-additive migration, surface morphology, and performance on injection moulded high-density polyethylene closures.* Journal of Colloid and Interface Science, 2017. **505**: p. 537-545.
33. Kunal Singha, M.S., *Fiber crimp distribution in nonwoven structure.* Frontiers in Science, 2013. **3**(1): p. 14-21.
34. Barach, J.L. and L.W. Rainard, *Effect of crimp on fiber behavior: part II: Addition of crimp to wool fibers and its effect on fiber properties.* Textile Research Journal, 1950. **20**(5): p. 308-316.
35. Hamad, S.F., *et al.*, *Low-voltage SEM of natural plant fibers: microstructure properties (surface and cross-section) and their link to the tensile properties.* Procedia Engineering, 2017. **200**: p. 295-302.
36. Riggott, J.M. and E.H. Wyatt, *Scanning electron microscopy of hair from different regions of the body of the rat.* Journal of Anatomy, 1980. **130**(Pt 1): p. 121-126.
37. Kenneth, D.L. and J.R. Thomas A. Kennedy, *The identification of specialty fibers.* Textile Research Journal, 1981. **51**(11): p. 703-709.

38. Adegbola, A., I.E.A. Aghachi, and O. Sadiku-Agboola, *SEM and AFM microscopical characterization of rPAN fibre and PET blends.* Alexandria Engineering Journal, 2018. **57**(1): p. 475-481.
39. Taloub, N., *et al.*, *Surface modification of PIPD fiber using nitric acid treatment.* Surface and Coatings Technology, 2018. **334**: p. 312-318.
40. Megelski, S., *et al.*, *Micro- and nanostructured surface morphology on electrospun polymer fibers.* Macromolecules, 2002. **35**(22): p. 8456-8466.
41. Sanjay, M.R., *et al.*, *Characterization and properties of natural fiber polymer composites: A comprehensive review.* Journal of Cleaner Production, 2018. **172**: p. 566-581.
42. Norambuena-Contreras, J., *et al.*, *Nanomechanical properties of polymeric fibres used in geosynthetics.* Polymer Testing, 2016. **54**: p. 67-77.
43. Skedung, L., *et al.*, *Feeling small: Exploring the tactile perception limits.* Scientific Reports, 2013. **3**: p. 2617.
44. Standardization, I.O.f., *ISO 9092:1988 Textiles Nonwovens Definition, 1988, Retrieved November 6th, 2018, https://www.iso.org/standard/16681.html*.
45. Schneider, C.A.R., W. S. & Eliceiri, K. W. , *NIH Image to ImageJ: 25 years of image analysis.* Nature methods 2012. **9(7)**: p. 671-675.
46. Ashiotis, G., *et al.* , *The fast azimuthal integration Python library: pyFAI.* Journal of Applied Crystallography,, 2015(48(2)): p. p. 510-519.
47. Karacan, I. and H. Benli, *An X-ray Diffraction study for isotactic polypropylene fibers produced with take-up speeds of 2500-4250 m/min*. Vol. 21. 2011. 201-209.
48. Favaro, M.M., M.C. Branciforti, and R.E.S. Bretas, *A X-ray study of ²-phase and molecular orientation in nucleated and non-nucleated injection molded polypropylene resins.* Materials Research, 2009. **12**: p. 455-464.
49. Kara, S., U.H. Erdogan, and N. Erdem, *Effect of polypropylene fiber cross sectional shapes on some structural/mechanical fiber properties and compressibility behaviour of plain knitted fabrics.* Fibers and Polymers, 2012. **13**(6): p. 790-794.
50. Schellbach, S.L., S.N. Monteiro, and J.W. Drelich, *A novel method for contact angle measurements on natural fibers.* Materials Letters, 2016. **164**(Supplement C): p. 599-604.
51. Huang, F., *et al.*, *Dynamic contact angles and morphology of PP fibres treated with plasma.* Polymer Testing, 2006. **25**(1): p. 22-27.
52. Della Volpe, C., *et al.*, *Air-plasma treated polyethylene fibres: effect of time and temperature ageing on fibre surface properties and on fibre-matrix adhesion.* Journal of Materials Science, 1994. **29**(15): p. 3919-3925.
53. Rebouillat, S., B. Letellier, and B. Steffenino, *Wettability of single fibres – beyond the contact angle approach.* International Journal of Adhesion and Adhesives, 1999. **19**(4): p. 303-314.
54. McHale, G. and M.I. Newton, *Global geometry and the equilibrium shapes of liquid drops on fibers.* Colloids and Surfaces A: Physicochemical and Engineering Aspects, 2002. **206**(1): p. 79-86.
55. Carroll, B.J., *The accurate measurement of contact angle, phase contact areas, drop volume, and Laplace excess pressure in drop-on-fiber systems.* Journal of Colloid and Interface Science, 1976. **57**(3): p. 488-495.
56. Committee, C.N.S.A., *Testing method for crimping performance of man-made staple fibres GB/T 14338-2008.*
57. Das, D., S.M. Ishtiaque, and S. Das, *Influence of fibre cross-sectional shape on air permeability of nonwovens.* Fibers and Polymers, 2015. **16**(1): p. 79-85.
58. Bhat Gajanan, S. and R. Malkan Sanjiv, *Extruded continuous filament nonwovens: Advances in scientific aspects.* Journal of Applied Polymer Science, 2001. **83**(3): p. 572-585.
59. Patel, R.M., *et al.*, *6 - Advances in polyolefin-based spunbond and binder fibres*, in *Polyolefin Fibres (Second Edition)*, S.C.O. Ugbolue, Editor. 2017, Woodhead Publishing. p. 157-185.

60. Tascan, M. and E.A. Vaughn, *Effects of total surface area and fabric density on the acoustical behavior of needlepunched nonwoven fabrics.* Textile Research Journal, 2008. **78**(4): p. 289-296.
61. Appel, D.W., Morman, M.T., *Method for forming nonwoven webs*. 1982, US4857251A.
62. Lloyd, D.R., K.E. Kinzer, and H.S. Tseng, *Microporous membrane formation via thermally induced phase separation. I. Solid-liquid phase separation.* Journal of Membrane Science, 1990. **52**(3): p. 239-261.
63. Givens, S.R., *et al.*, *High-temperature electrospinning of polyethylene microfibers from solution.* Macromolecules, 2007. **40**(3): p. 608-610.
64. Wang, Y., *et al.*, *Novel nanoscale topography on poly(propylene carbonate)/poly(ε-caprolactone) electrospun nanofibers modifies osteogenic capacity of ADCs.* RSC Advances, 2015. **5**(101): p. 82834-82844.
65. Kumar, S., *et al.*, *Method of extruding a single polymeric fiber.* 1992.
66. Ogawa, T., H. Mukai, and S. Osawa, *Effects of functional groups and surface roughness on interfacial shear strength in ultrahigh molecular weight polyethylene fiber/polyethylene system.* Journal of Applied Polymer Science, 1999. **71**(2): p. 243-249.
67. Boyer, R.F., *Glassy transitions in semicrystalline polymers.* Journal of Polymer Science: Polymer Symposia, 1975. **50**(1): p. 189-242.
68. Pilkington, G., *et al.*, *Amontonian frictional behaviour of nanostructured surfaces.* Physical Chemistry Chemical Physics, 2011. **13**(20): p. 9318-9326.
69. Quignon, B., *et al.*, *Sustained frictional instabilities on nanodomed surfaces: stick–slip amplitude coefficient.* ACS Nano, 2013. **7**(12): p. 10850-10862.
70. Hansson, P.M., *et al.*, *Frictional forces between hydrophilic and hydrophobic particle coated nanostructured surfaces.* Physical Chemistry Chemical Physics, 2013. **15**(41): p. 17893-17902.
71. Tanford, C., *Micelle shape and size.* The Journal of Physical Chemistry, 1972. **76**(21): p. 3020-3024.
72. Leiserowitz, L. and G.M.J. Schmidt, *Molecular packing modes. Part III. Primary amides.* Journal of the Chemical Society A: Inorganic, Physical, Theoretical, 1969(0): p. 2372-2382.
73. Nigmatullin, R., et al., *Mechanically Robust Gels Formed from Hydrophobized Cellulose Nanocrystals.* ACS Applied Materials & Interfaces, 2018. **10**(23): p. 19318-19322.
74. Nigmatullin, R., et al., *Thermosensitive supramolecular and colloidal hydrogels via self-assembly modulated by hydrophobized cellulose nanocrystals.* Cellulose, 2019. **26**(1): p. 529-542.
75. Swift, T.A., et al., *Surface functionalisation significantly changes the physical and electronic properties of carbon nano-dots.* Nanoscale, 2018. **10**(29): p. 13908-13912.
76. Terry, C., et al., *Structural features distinguishing infectious ex vivo mammalian prions from non-infectious fibrillar assemblies generated in vitro.* Scientific Reports, 2019. **9**(1): p. 376.
77. Fox, H.W. and W.A. Zisman, *The spreading of liquids on low-energy surfaces. III. Hydrocarbon surfaces.* Journal of Colloid Science, 1952. **7**(4): p. 428-442.
78. Mizes, H., *et al.*, *Submicron probe of polymer adhesion with atomic force microscopy: dependence on topography and material inhomogeneities.* Applied physics letters, 1991. **59**(22): p. 2901-2903.
79. Hossain, M., M. Acar, and W.J.P.o.t.I.o.M.E. Malalasekera, Part E: Journal of Process Mechanical Engineering, *A mathematical model for airflow and heat transfer through fibrous webs.* 2005. **219**(4): p. 357-366.
80. Peksen, M., M. Acar, and W.J.P.o.t.I.o.M.E. Malalasekera, Part E: Journal of Process Mechanical Engineering, *Computational modelling and experimental validation of the thermal fusion bonding process in porous fibrous media.* 2011. **225**(3): p. 173-182.
81. Huang, Y., et al., *Single-crystalline 2D erucamide with low friction and enhanced thermal conductivity.* Colloids and Surfaces A: Physicochemical and Engineering Aspects, 2018. **540**: p. 29-35.